# Modelling and experiments to identify high-risk failure scenarios for testing the safety of lithium-ion cells

Donal P. Finegan[a,*], John Darst[b], William Walker[b], Qibo Li[a], Chuanbo Yang[a], Rhodri Jervis[c], Thomas M.M. Heenan[c], Jennifer Hack[c], James C. Thomas[b], Alexander Rack[d], Dan J.L. Brett[c], Paul R. Shearing[c], Matt Keyser[a], Eric Darcy[b]

[a] National Renewable Energy Laboratory, 15013 Denver W Parkway, Golden, CO, 80401, USA
[b] NASA Johnson Space Center, 2101 E NASA Pkwy, Houston, TX, 77058, USA
[c] Electrochemical Innovation Lab, Department of Chemical Engineering, University College London, London, WC1E 7JE, UK
[d] The European Synchrotron (ESRF), 71 Avenue des Martyrs, 38000, Grenoble, France

## ARTICLE INFO

## ABSTRACT

Intentionally inducing worst-case thermal runaway scenarios in Li-ion cells on-demand is a definitive way to test the efficacy of battery systems in safely mitigating the consequences of catastrophic failure. An internal short-circuiting (ISC) device is implanted into three 18650 cell designs: one standard, one with a bottom vent, and one with a thicker casing. Through an extensive study of 228 cells, the position at which thermal runaway initiates is shown to greatly affect the tendency of cells to rupture and incur side-wall breaches at specific locations. The risks associated with each failure mechanism and position of the ISC device are quantified using a custom calorimeter that can decouple the heat from ejected and non-ejected contents. Causes of high-risk failure mechanisms, such as bursting and side-wall breaches, are elucidated using high-speed synchrotron X-ray imaging at 2000 frames per second and image-based 3D thermal runaway computational models, which together are used to construct a comprehensive description of external risks based on internal structural and thermal phenomena.

## 1. Introduction

The continued widespread adoption of lithium-ion (Li-ion) batteries for a plethora of applications, from e-cigarettes to manned-spacecraft, is accompanied by an urgent need for effective safety testing strategies. One sure way of knowing that a battery system is 'safe' is by testing its response to the 'worst-case' failure scenarios. A Li-ion battery can fail catastrophically when a process known as 'thermal runaway' occurs. That is, at a critical temperature and in the presence of non-aqueous liquid electrolytes and oxygen [1], the active materials within a Li-ion battery can exothermically react [1–4]. Exothermic reactions can become self-sustaining when local heat generation is greater than heat dissipation, resulting in violent combustion and total cell failure. During thermal runaway, it has been estimated that about 2 L of gas is generated per amp hour (Ah) of commercial $LiFePO_4$ and $LiNi_xCo_yAl_zO_2$ 18650 cells [5]. Modern 18650 cells have capacities greater than 3 Ah, and can generate more than 6 L of gas within *ca.* 2 s during thermal runaway, which is mostly flammable [1]. In this short time ($< 2$ s), more than 70 kJ of heat can also be generated [6] and surface

temperatures greater than 600 °C can be reached [7,8]. Avoiding a hazardous pressure build-up and violent ruptures [9], as well as safely dissipating the heat during this period, poses considerable challenges, both in the design of single cells and complete battery systems. If heat and pressure are not safely managed during thermal runaway, side-wall breaches can occur, where the casing of a cell is breached either by thermally-induced melting or by pressure-induced splits. Side-wall breaches are most catastrophic for cells encased in a rigid material such as the steel container used in 18650 cells. Such side-wall breaches present an alternate path for pressure relief in the form of an ignited flare of flammable product gases and electrolyte. When side-wall breaches and flares occur, they can often defeat interstitial heat-sink materials and impinge neighboring cells directly, leading to propagation of thermal runaway from cell to cell [6,10], and hence present the greatest challenge in preventing propagation.

The occurrence of a side-wall breach is widely considered to be among the 'worst-case' failure scenarios. For mission critical applications (e.g. the battery pack of the NASA spacesuit life-support system), all practical measures must be taken to minimize/eliminate the risk of

---

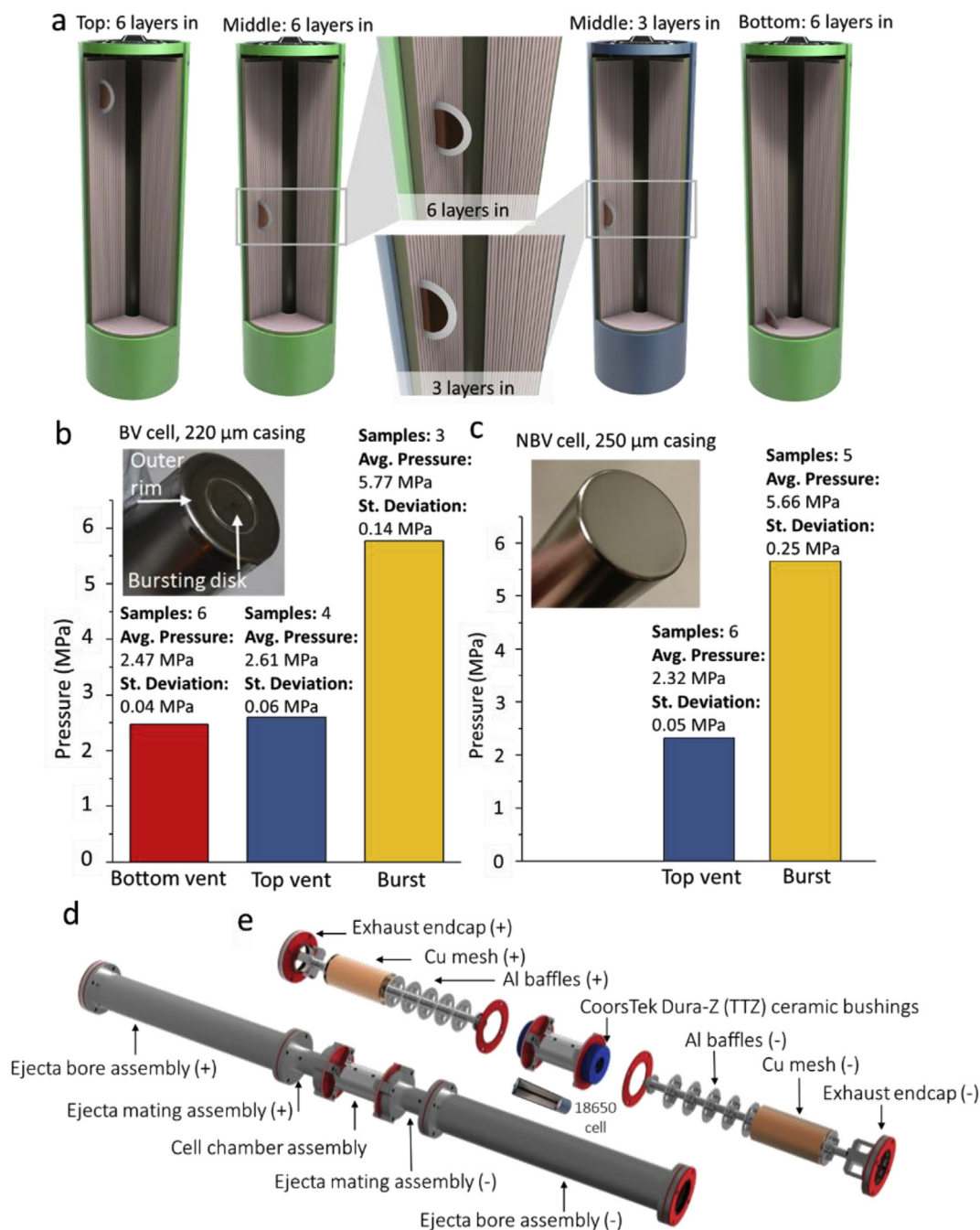**Fig. 1.** (a) Illustrations showing the various positions of the ISC device in the test-cells. (b) Plot showing the pressure at which the bottom and top (CID) vents activate and the cell bursts, for cells with a bottom vent feature. The bottom vent is shown in the inset photograph. (c) Plot showing the pressure at which the top vent (CID) activates and the cell bursts for cells without a bottom vent. The inset photograph shows the base of the cell without a bottom vent. (d) Illustration showing an external view of the assembled fractional thermal runaway calorimeter (FTRC) and (e) illustration showing a view of the internal components of the FTRC, highlighting the insulating ceramic bushings (blue) between the cell and ejecta chambers, as well as the components inside the bore chamber that capture the heat from escaping gases and debris. (For interpretation of the references to color in this figure legend, the reader is referred to the Web version of this article.)

catastrophic failure. Rigorous abuse testing is carried out to identify vulnerabilities of the battery system. Where possible, it is prudent to reproduce failure scenarios that will most challenge conceivable vulnerabilities within the battery system. This might require, for example, the ability to reliably control when and where (for orienting towards adjacent cells) side-wall breaches occur in high energy density cells. Currently, when the efficacy of a module in preventing propagation of thermal runaway is tested, an individual cell is most often failed by either applying a patch heater [11] or by nail penetration [12–14]. Both methods have limitations. Surface heating and nail penetration can only

be applied to relatively simple pack configurations [11,14] and neither method can reliably induce worst-case failure scenarios. For example, nail penetration has previously been shown to lead to less violent thermal runaway events due to the nail pinning the electrode assembly inside the casing, the nail acting as a heat sink, spreading the short-circuit across a large area, and creating an additional path for pressure relief [12]. Surface heating via patch heaters, or otherwise, lacks control of the location where thermal runaway will initiate [8], requires additional space and wiring, affects the structural integrity of the casing, and takes minutes of heating to reach the critical temperature of

thermal runaway providing more time for the electrode assembly to dry following initial venting. Drying of the electrode assembly also occurs for other testing methods such as oven tests [15] or accelerating rate calorimetry [7,16,17]. For complex battery systems, where accessibility for abuse testing is challenging, safety-focused computational models are crucial for predicting outcomes of a single cell undergoing thermal runaway inside a system [18,19]. However, the predictive capability of a model is dependent upon the accuracy of the experimental measurements used to inform the model parameters [20,21], adding further incentive to facilitate a method of inducing 'worst-case' thermal runaway scenarios in complex systems, and subsequently recording the data for further modelling analyses.

The ideal scenario for maximizing the heat output from a cell is for it to undergo a hard internal-short circuit, such that thermal runaway initiates and begins to propagate instantaneously without allowing time for the electrolyte to vent and escape the system. There have been numerous approaches used to trigger internal short circuits inside cells on demand [10,22,23]. In this work, we use an internal short circuiting (ISC) device that utilizes a low melting point wax to create, on-demand, an internal short circuit between the Al positive current collector and the surface of the graphite negative electrode [10]. This type of short circuit is considered to be the most likely to induce thermal runaway as it connects two highly electrically conducting materials where the heat dissipation for the graphite material is relatively low due to its porous architecture [10,24]. This ISC device is selectively positioned within 18650 test-cells to determine the influence of the location of failure initiation on the risk of certain unfavorable failure mechanisms, such as bursting and local side-wall breaches. In an extensive study of 228 cells, the risks associated with each location of the ISC device are compared by assessing the probability that the cell undergoes bursting or breaching at a particular location. Three test-cell designs are compared: a standard 18650 cell, an 18650 cell with a bottom vent, and an 18650 cell with a thicker casing. In addition to considering the probability of a cell to burst or breach, risks are assessed based on their surface temperature profiles and the total quantity as well as fractions of heat generated from ejected and non-ejected materials. High-speed synchrotron X-ray imaging is used to capture the internal structural dynamics, allowing, for the first time, internal events to be linked to external risks. The thermal and radiography data are used to inform a computational thermal runaway model for an 18650 cell elucidating both dynamic internal and surface temperatures, yielding a quantitative description of regions that are most susceptible to breaching. This work also marks the first time that real-time internal dynamics of a cell undergoing thermal runaway are used to inform a computational model.

## 2. Experiment

### 2.1. Preparation of cells

To determine the location where the initiation of thermal runaway poses the greatest external risk, an internal short-circuiting (ISC) device, developed between NASA and NREL [10,25], was integrated into 18650 test-cells at 6 different locations within the cells: 6 or 3 layers deep, and at the top, middle or bottom of the electrode assembly (Fig. 1). All cells passed a < 5% self-discharge from 100% SOC over 3 months. The ISC device is designed to mimic the effect of a defect inside the electrode assembly causing a short, and herein creates a short circuit between the positive current collector and the graphite active material on the negative electrode, which is deemed the most likely type of short for the initiation of thermal runaway [24]. Dimensions and details surrounding the construction of the ISC device are provided in a previous study [10]. The internal short occurs when the ISC device reaches 57 °C, the wax interface between the positive and negative sides melts, and the winding tension of the electrode assembly compresses the layers resulting in a conducting path.

The 18650 test-cells utilized herein had capacities of 3.35 Ah, an

NMC positive electrode, graphite negative electrode, and were each charged to 100% SOC (4.2 V) before testing. All cell designs had a mass between 47.0 g and 47.8 g, and had a diameters < 18.15 mm. Test-cells with and without an implanted ISC device were tested and compared. Three casing designs were also tested; one with a bottom vent (BV) feature (inset in Fig. 1b) and one without (inset of Fig. 1c) where both cells had a 220 μm thick casing. The third design was a non-bottom vent (NBV) cell with 250 μm thick casing. All other features of the cells (chemistry, electrode assembly, header design, etc.) were identical. The bottom vent consists of weakened annulus on the base plate that acts as a bursting disk, and is designed to rupture at a pressure between the bursting pressure of the current interrupt device (CID) and the pressure required to extend the spin-groove and lead to ejection of contents [9]. The pressures required to activate the CID, bottom vent, and to extend the spin groove were tested by cutting the 18650 cells mid-way along the cell longitudinally, sealing the remaining half (top or bottom) into a mechanical fitting with epoxy, and slowly increasing the pressure until the device activated. To test the pressure at which the spin-groove extends and the cell bursts, an additional step of blocking the CID with epoxy was required. The activation pressures of each pressure relief mechanism for the test-cells are shown in Fig. 1b–c where all tests were carried out at room temperature.

### 2.2. Calorimetry

To determine the risks associated with overall heat generation and the distribution of heat generated from ejected and non-ejected materials, calorimetry was carried out in a custom-designed fractional thermal runaway calorimeter (FTRC) that can decouple the heat output from the casing of cells and ejected contents (Fig. 1d and e). The FTRC was designed to capture and isolate the heat from contents ejected from the top and bottom of 18650 cells and was described in detail in a previous study by the authors [6]. The 18650 cells were placed inside an aluminum cell chamber assembly that was thermally isolated from the ejecta mating and ejecta bore assemblies in which a system of Al baffles and Cu mesh capture the heat from ejecting gas and solids, thereby enabling the decoupling of heat from the cell casing conduction and ejecta. The cell chamber was heated using four heating cartridges supplied with 1 kW of continuous power (at 250 V and 4 A) until the cell underwent thermal runaway. For cells containing an ISC device, thermal runaway typically occurred within *ca.* 40 s of heating, whereas cells without an ISC device typically took *ca.* 90 s. Upon thermal runaway, the power supply was immediately switched off and the subsequent heat stemming from the cell and its ejected content continued to heat the system. The heat from each component of the calorimeter was calculated based on the temperature response of each component, allowing quantification of the total heat output, as well as the fractions of heat that arose from the cell, contents ejected from the top of the cell, and contents ejected from the bottom of the cell. As the calorimeter is composed of aluminum, which only weakly attenuates high energy X-rays, simultaneous high-speed X-ray imaging was carried out, allowing heat generation and temperatures to be characterized with respect to internal phenomena.

### 2.3. Stand-alone tests and thermal imaging

To identify the risks associated with hot-spots and flares, tests were carried out in an open environment inside a containment system (described in previous work [9,10]) with infra-red-transparent sapphire windows for simultaneous high-speed thermal imaging during X-ray imaging experiments. The cells were heated using a NiCr heating wire wrapped circumferentially near their base. A thin coat of thermally conductive ceramic putty (Cotronics 950) was applied to the cell base to adhere a layer of fireproof mica tape, which was placed between the high-resistance wire and the surface of the 18650 cells, the wire was then coated in electrically isolating ceramic putty (Cotronics 907 GF)

and allowed to set. Finally, an additional wrap of Mika tape was applied. A gap of *ca.* 2 mm between the bottom of the heating fixture and the base of the cell was left for the cell to be secured in place by a shaft collar (photograph included in Supplementary Information). The two-piece shaft collar applied equal and constant pressure circumferentially. Inside the containment system the shaft collar was held in place by hydraulic clamps that kept the cell inside the field of view for thermal and X-ray imaging. The cells were held mid-air at *ca.* 15 mm above the surface of the containment to allow successful activation of the BV and subsequent ejection. Most cells described herein were tested at a synchrotron facility using this setup, but, due to time being limited at the synchrotron facilities, further tests were carried out at the NASA Johnson Space Center to improve statistical significance of observations. These tests involved non-ISC cells only (with and without BVs), and were conducted in an oven set at 250 °C.

The surface temperature of the cells was measured using a thermal camera (FLIR SC5000MB, FLIR Systems France, Croissy-Beaubourg, France) which had an InSb detector that was sensitive to wavelengths between 2.5 μm and 5.1 μm. The thermal camera was operated in its high temperature range, covering from 200 °C to 1500 °C, for which the noise equivalent temperature difference was < 20 mK and the measurement accuracy was ± 1% of the measured temperature in degrees Celsius. The thermal camera was situated *ca.* 30 cm from the cell behind a 2 mm thick infra-red transparent sapphire window. Images were recorded at 50 Hz, which allowed a high temporal resolution of the spatial surface temperature profiles. The 18650 cells were painted in a heat-resistant black paint which had a calibrated emissivity [26] of 0.96 over the range of 50–200 °C.

### 2.4. X-ray imaging

High-speed X-ray imaging was carried out at beamline ID19 at The European Synchrotron (ESRF). The cells were imaged under a polychromatic beam with a pixel size of 11.35 μm and varying fields-of-view (FOV) and frame rates, from 2000 fps with a FOV of 1822 × 1140 pixels (horizontal × vertical), to 9141 fps with a FOV of 1616 × 316 pixels (horizontal × vertical). A PCO.Dimax (PCO AG, Germany) detector and LuAG(Ce) ($Lu_3Al_5O_{12}$:Ce) scintillator were used for all high-speed imaging experiments. The radiographs were flat-field corrected and enhanced using MATLAB's adaptive histogram equalization (adapthisteq) function. Imaging properties and post-processing were similar to previous studies [9,10,12].

### 2.5. Modelling

Thermal runaway involves multi-physics behavior. An integrated model is used to explore interplays between chemical, thermal, electrical characteristics, environmental conditions, and types of faults. A multi-scale multi-physics Li-ion cell model is employed to address the three-dimensional spatial impact of an internal short circuit. The modelling tool, based on the multi-scale multi-domain (MSMD) modelling framework [27], has a modularized hierarchical architecture, allowing independent choice of sub-models. To address the response of a Li-ion cell to an internal short circuit, three component models are integrated into the MSMD tool to compute instant heat generation: localized short-circuit current and accompanying joule heat at shorted cell volume, cell-wide current flow and corresponding electrochemical heat, and exothermic decomposition reactions at elevated temperature [28]. Therefore, the local heat generation rate, $\bar{q}_x''$, is a sum of heat fluxes from each of the component models (Eq. (1)).

$$\bar{q}_x'' = \bar{q}_{x,ech}'' + \bar{q}_{x,ark}'' + \bar{q}_{x,srt}''$$ (1)

Where, $\bar{q}_{x,ech}''$ includes ohmic heat and electrochemical heat, $\bar{q}_{x,ark}''$ is the heat from high temperature decomposition reactions, and $\bar{q}_{x,srt}''$ represents the heat generated from ohmic loss through the short circuit. A

plot of the time-dependent individual contributions of each heat source is provided in Supplementary Material. A 3D model was constructed using parameters drawn from the actual 3.35 Ah 18650 cells utilized herein and are summarized in Supplementary Information. The reaction rate equations and modelling parameters used herein are provided in Supplementary Information. Three simulations were carried out corresponding to the three positions of the ISC device shown in Fig. S2 of Supplementary Material. The current model does not account for mass loss during the process of thermal runaway.

When the temporal surface temperatures were generated for the three simulations, an additional step of applying temperature-dependent tensile strength properties of the casing was applied to estimate the bursting pressure of the casing. The tensile strength as a function of temperature of a common structural steel (S350GD) [29] was used, the data and functions for which are provided in Supplementary Information. The burst pressures were estimated using Barlow's formula (Eq. (2)), which calculates the bursting pressure ($P$) from the ultimate tensile strength of the casing material ($S$), the thickness of the casing ($t$), and the outer diameter ($D$).

$$P = 2\frac{St}{D}$$ (2)

## 3. Results and discussion

### 3.1. Overview of testing results

The 'worst-case' failure mechanism is broadly considered to be the type of failure that leads to the most hazardous, costly, and catastrophic outcome. This can be classified as a function of safety and economics, where the specific application determines how each factor is weighed. Here, we consider phenomena at the cell level that occur during thermal runaway and may lead to the most unfavorable or 'worst-case' outcome. The primary factors of concern during failure are the thermal behavior of the cell and its propensity to undergo an uncontrolled ejection of hot, electrically conducting material. Both the thermal behavior and the propensity of 18650 cells to undergo uncontrolled ejection are considered here. The location and vector of the ejection determines the associated risks. For example, a side-wall breach might lead to the most hazardous and costly failure by incurring the highest risk of causing cell-to-cell propagation inside a module. Here, we use the term 'bursting' to describe when an ejection is 'uncontrolled' and involves the header components of the cell being released from the main casing, which is often accompanied by the internal electrode assembly escaping as a single projectile. Whereas during 'controlled' ejection, the header components remain in place and the fluidized internal materials escape through the vent ports avoiding the formation of projectiles. Hence, similar amounts of mass may be released during controlled and uncontrolled ejections, but the mechanisms, rate, and consequences of the mass release differ. Uncontrolled ejection is thus further classified into five different types, examples of which are shown in Fig. 2a:

1. Bursting through the top
2. Bursting through the bottom (mostly applicable to BV cells)
3. Casing breach near the top
4. Casing breach on the side
5. Casing breach near the bottom

Oxidation-induced discoloration on the surface of casings was also treated as an indicator that the discolored region incurred significant thermal stress and may have an increased susceptibility to thermal-induced breaches (e.g. see Fig. 2b). The likelihood of a single cell design to undergo one of the five failure types is expected to be strongly dependent on the internal phenomena during thermal runaway, such as the location of thermal runaway initiation. To test this, an experimental
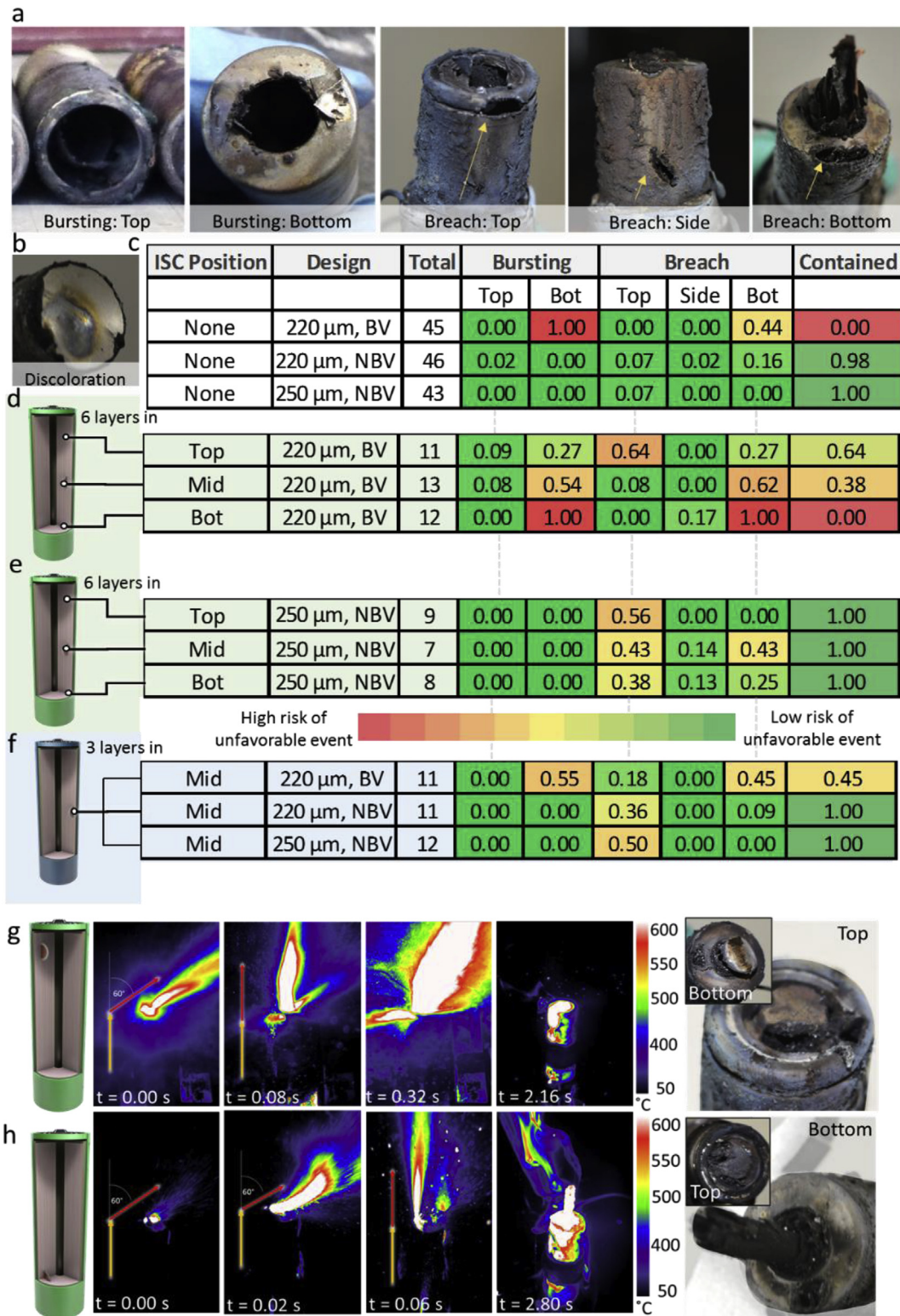
**Fig. 2.** (a) Photographs showing examples of specified failure mechanisms. (b) Discoloring that can occur at high-risk regions when a breach does not form. (c) Table showing the fraction of non-ISC BV and NBV cells with 220 μm and 250 μm casing thicknesses that underwent bursting and breaches. The number in the colored boxes is the fraction of the total cells tested that underwent the specified failure mechanisms. The fraction of cells that contained the entire process of thermal runaway without bursting is also shown. (d) Table showing the behavior of cells that had an ISC device integrated 6 layers deep at three different longitudinal locations for BV cells with a 220 μm casing and (e) for NBV cells with a 250 μm casing. (f) Equivalent table for cells with an ISC device integrated 3 layers deep. (g–h) Time stamped sequence of thermal images taken during thermal runaway, and photographs showing the top and bottom vents of the cell for (g) a cell where the top vent is facing up, that incurred a top breach where the ISC device was located near the top and (h) a cell where the bottom vent is facing up, that incurred a bottom breach where the ISC device was located near the bottom. The yellow and red arrows in the thermal images indicate the orientation of the cell and the direction of the venting flare, respectively. Thermal imaging movies for (g) and (h) are provided as Supplementary Movies 1 and 2. (For interpretation of the references to color in this figure legend, the reader is referred to the Web version of this article.)

matrix where several cells are tested for a range of different locations of initiation was constructed for BV and NBV 18650 cells, as shown in Fig. 2b, and for two different casing thicknesses (220 and 250 μm). The ISC device enabled control of when and where thermal runaway would initiate within the cell and was placed at the four different locations shown in Fig. 1a. Standard cells without ISC devices were also tested for comparison. The results of this extensive study of 228 cells are summarized in Fig. 2c–f. The number in the colored boxes in Fig. 2c–f is the fraction of the total cells tested that underwent the specified failure mechanisms. Color-coding in Fig. 2c–f is set to help qualitatively convey unfavorable events. Cells tested in Fig. 2c–f were sometimes oriented differently but were always in an environment that facilitated ejection from both ends of the cell. Orientation is not thought to affect the failure mechanisms, as internal pressure-induced dynamics are expected to far outweigh any gravitational affects from different orientations.

*Risks for standard (non-ISC) cells:* For standard non-ISC cells (Figs. 2c), 100% of the bottom vents activated on the BV cells with 220 μm casings, of which 44% were accompanied by a bottom breach. In comparison, the equivalent NBV cell showed a lower risk (16%) of a bottom breach occurring, but an increased risk of top bursting (2%) and top breaches (7%). This indicates that the BV helps mitigate the risk of cells bursting or breaching at the header via improved pressure relief and reduced strain on the header components during thermal runaway. BV cells demonstrated an increased risk of bottom breaches when compared to their NBV counterparts. The thick casing (250 μm) NBV cells demonstrated a reduced risk of bottom breaches occurring (0%) than the thinner 220 μm casing cells, but a similar risk of top breaches occurring (7%). The thick casing cells were shown to have a reduced risk of breaches occurring overall, which is most likely due to increased mechanical strength and improved heat dissipation on the casing.

*Influence of longitudinal location of initiation on risks:* For the 220 μm BV cells, the position of the ISC device was 6 layers deep and varied longitudinally (top, middle, and bottom). The longitudinal location of the ISC device, and hence the location of initiation of thermal runaway, was shown to drastically affect the failure mechanism of the cell (Fig. 2d). Cells with an ISC device placed near the top had a much higher risk of top bursting (9%) and top breaches (64%) than cells where the ISC device was placed near the bottom, where 0% of cells underwent top bursting and top breaching. Conversely, when the ISC device was placed near the bottom, 100% of cells underwent bottom bursting and breaching, whereas 0% of cells underwent top bursting and breaching. Placing the ISC device near the bottom also showed the highest risk of side-wall breach (17%). Placing the ISC device in the middle consistently demonstrated intermediate behavior, where 8% of cells underwent top bursting and breaches, and 54% and 62% of cells underwent bottom bursting and bottom breaching, respectively. In summary, the proximity of the ISC device to either end of the 18650 cells significantly increased the risk of bursting and/or breaching occurring at that end. For all cases, breaching at the top, middle, and bottom, occurred on the side where the ISC device was placed illustrating that the ISC device provides longitudinal as well as circumferential control of where a breach is likely to occur.

*Influence of radial location of initiation on risks:* The influence of the radial position of the ISC device on the failure mechanism was investigated by placing the ISC device 6 or 3 layers deep near the middle of 220 μm BV and NBV cells, as well as 250 μm NBV cells (Fig. 2f). Comparing the 220 μm BV cell with the ISC device 6 or 3 layers deep, a slight increase in the risk of a top breach occurring (from 8% for 6 layers to 18% for 3 layers) and a slight decrease in the risk of bottom breach (from 62% for 6 layers to 45% for 3 layers) are observed. Like the non-ISC cells, the 220 μm and 250 μm NBV cells showed a reduced risk of bottom bursting (0%) and bottom breach (9% and 0%, respectively), for cells with the ISC 3 layers deep.

*Influence of thicker casings and bottom vents on risks:* NBV cells with a thicker casing (250 μm) were shown to be more resilient against

top bursting than their 220 μm counterparts, where 0% of the 250 μm cells tested burst (Fig. 2e). A strong dependence was observed between the location of the ISC device and the 250 μm cell's propensity to undergo breaches. The percentage of NBV cells that underwent top breaches for the ISC device placed at the top, middle and bottom, were 56%, 42%, and 38% respectively, decreasing in risk as the distance of the ISC device from the top increased. NBV cells with the ISC device located at the middle showed the highest risk of side and bottom breaches, with 14% and 43% respectively. Comparing the results in Fig. 2c–e, it is observed that inclusion of the bottom vent leads to a reduced risk of top bursting and breaching overall but increases the risk of bottom bursting and breaching. The increase in casing thickness from 220 μm to 250 μm is shown to have reduced the risk of bursting at the top and bottom, and, as observed in Fig. 2c, reduces the risk of breaching. Almost all the NBV cells that did not undergo a bottom breach showed discoloration due to oxidation of the steel casing at elevated temperatures (Fig. 2b) on the base plate on the side clocked with the circumferential position of the ISC device.

The location of the ISC device greatly influenced the propensity of cells to incur high risk failure mechanisms, such as bursting or breaches, at certain locations along the surface of the casing. To explain the external risks with respect to internal phenomena, the external temperature profiles and internal structural dynamics that lead to breaching are examined in the following section.

Supplementary video related to this article can be found at https://doi.org/10.1016/j.jpowsour.2019.01.077.

### 3.2. Identifying the cause of breaches

The position of the ISC device and hence the location of thermal runaway initiation clearly influences the risk and nature of the breaches along the casing of the cell (Fig. 2). The underlying thermal and structural dynamics that contribute to the relationship between location of failure initiation and risk of breaches is explored via a combined approach of high-rate thermal imaging (50 fps) and high-speed X-ray imaging (> 2000 fps). In this section, the risk map shown in Fig. 2 is explained with respect to surface temperatures and dynamic internal phenomena.

*External phenomena:* Two typical examples of a top breach and bottom breach that occur for the ISC device positioned at the top and bottom, respectively, are shown in Fig. 2. As observed in the thermal images in Fig. 2g and h, within the first 0.08 s of initiation, the venting flare is shown to deflect at an angle of about 60° from vertical, which is highlighted by the red arrows. In the case of the top vent breach (Fig. 2a), the flare appears to deflect off the spin-groove and top button. In the case of the BV breach (Fig. 2b) the flare appears to deflect off the outer rim of the base plate following activation of the BV. After *ca.* 0.08 s, the flare melts through the material off which it was deflected, and changes to a vertical direction. In every instance, the breach occurred on the side of the ISC device directly above or below its position. The breach is shown in the post-mortem photographs in Fig. 2g and h, and as seen in the inset photograph of the opposite side, there is also observable damage on the side aligned with the location of the ISC device.

*Internal phenomena:* High-speed X-ray imaging during thermal runaway of the cells enabled the linking of external observations with internal events, with high temporal resolution. Fig. 3a and b, show the events leading up to the breach of the cells presented in Fig. 2g and h, respectively. The formation of a breach in the casing of the cell is seen as a dark shadow expanding, which indicates that the steel casing in that region was melting away and a gap was opening. The formation of the breach is most clearly seen in the Supplementary Movies 3 and 4, where its progression is relatively eye-catching compared to the static images presented in Fig. 3. To help with identifying the progression of the breaches in Fig. 3, the features are highlighted using red circles and arrows. In Fig. 3a, the ISC device was placed 6 layers deep near the top
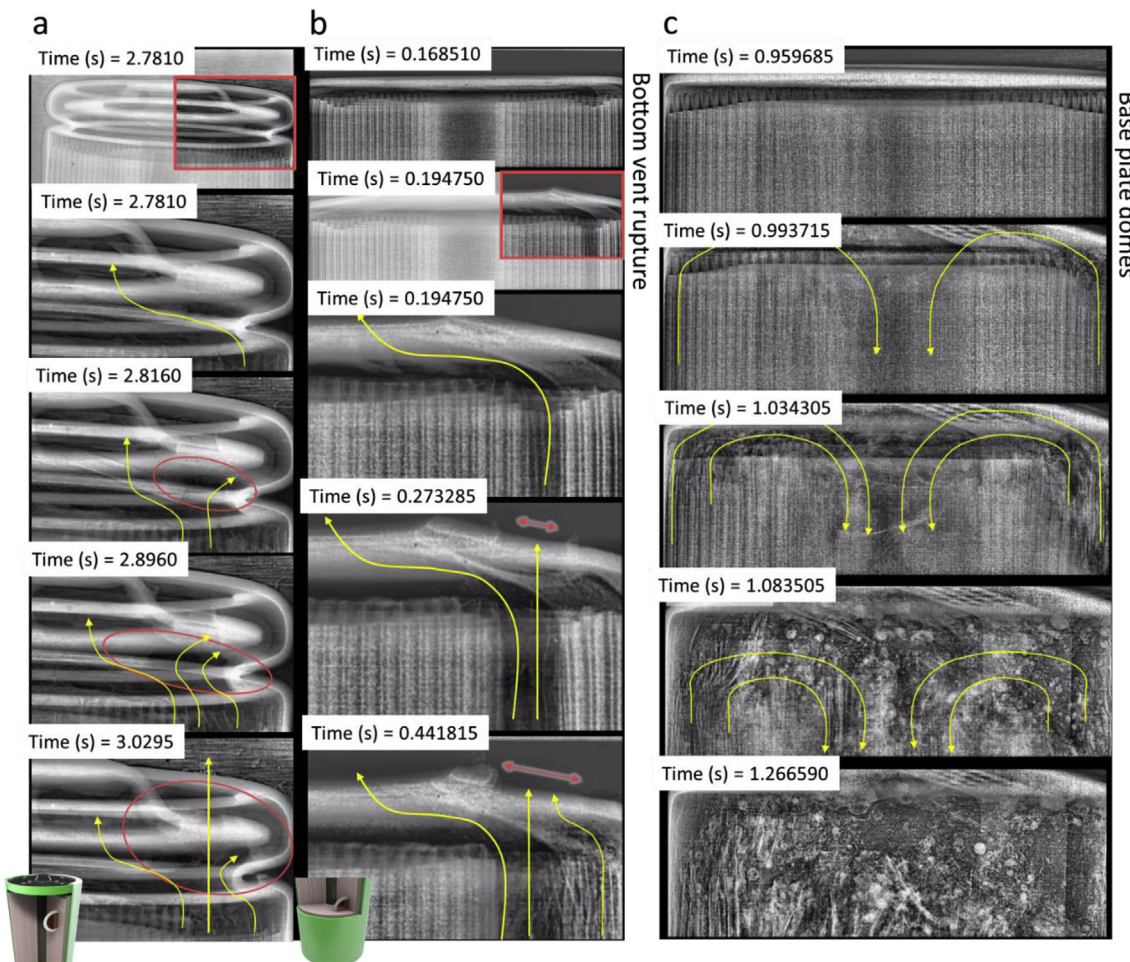
**Fig. 3.** Time-stamped radiographs showing (a) the top of a cell with ISC device located 6 layers deep at the top, where the region highlighted by the red circle shows a hole forming on the spin-groove through which the ejecting material flowed, as highlighted by the yellow streamlines; (b) a breach forming on the outer rim of the base of a BV cell with ISC device placed near the bottom, where the red arrows highlight the opening breach and yellow streamlines highlight the change in direction of ejecting material; (c) the base of an NBV cell without an ISC device, showing how the ejecting material first deflects off the base plate before ejecting through the core of the electrode assembly. Movies of (a), (b), and (c) are provided as Supplementary Movies 3, 4, and 5. (For interpretation of the references to color in this figure legend, the reader is referred to the Web version of this article.)

of the cell, and the cell was oriented such that the ISC device was parallel with the field-of-view on the right side of the image. Upon initiation of thermal runaway, the active material broke down and ejected with fluid-like properties. The observable flow of the fluidized reacting material in Supplementary Movies 3 and 4 is represented as yellow streamlines in Fig. 3. In Fig. 3a, the flow of ejecting material is first seen to deflect off the spin-groove and pass out through the vent. This region of deflection experienced increased thermal stress due to enhanced convective heat transfer and was thus a region that was relatively more susceptible to weakening, melting, and undergoing a breach. The spin-groove initially melted, soon followed by the top-fold holding the header components, allowing the molten material to flow unimpeded vertically out of the cell. This change in flow direction is seen externally between 0.00 s and 0.08 s in Fig. 2g.

Supplementary video related to this article can be found at https://doi.org/10.1016/j.jpowsour.2019.01.077.

Similarly, after the BV activated, the ejecting fluidized materials initially deflected off the outer rim and passed out through the vent (Fig. 3b). The region at which the material deflected melted within *ca.* 0.1 s and the melted hole continued to widen over *ca.* 0.15 s. The direction of flow, as illustrated by the yellow streamlines in Fig. 3b, changed from curving around the outer rim to passing directly through the outer rim, a change that is observed in the thermal images between 0.02 s and 0.06 s in Fig. 2h. As seen in Fig. 2, cells without a BV were

much less likely to undergo a bottom breach than BV cells. In Fig. 3c (Supplementary Movie 5), the internal structural dynamics of an NBV cell without an ISC device are shown. The yellow streamlines show that the broken-down fluidized material initially flowed towards the base plate of the cell, but took a 180° turn towards the top vent due to the pressure drop through the vacant core of the electrode assembly. The base plate still acted as a point of deflection (hence the frequent discoloration shown in Fig. 2b) but was not as susceptible to breaches forming. This may be due to the complete base plate acting as a better heat sink than the base plate with a BV missing, and helping to dissipate heat and mitigate the formation of hot spots. Note that for BV cells, the bottom breach occurred in addition to the bottom vent rupture, that is to say, there were two separate holes in the base of the cell, one from the bottom vent, and one breach hole on the remaining annulus.

Supplementary video related to this article can be found at https://doi.org/10.1016/j.jpowsour.2019.01.077.

### 3.3. Thermal behavior of cells and vulnerabilities

In determining the 'worst-case' location of failure initiation, the thermal behavior of the cell is a crucial aspect to consider. The surface temperature of the cell is what determines the necessary properties of the cell casing to avoid ruptures; i.e. high temperatures lead to lower tensile strengths and increased susceptibility to breaching or bursting.
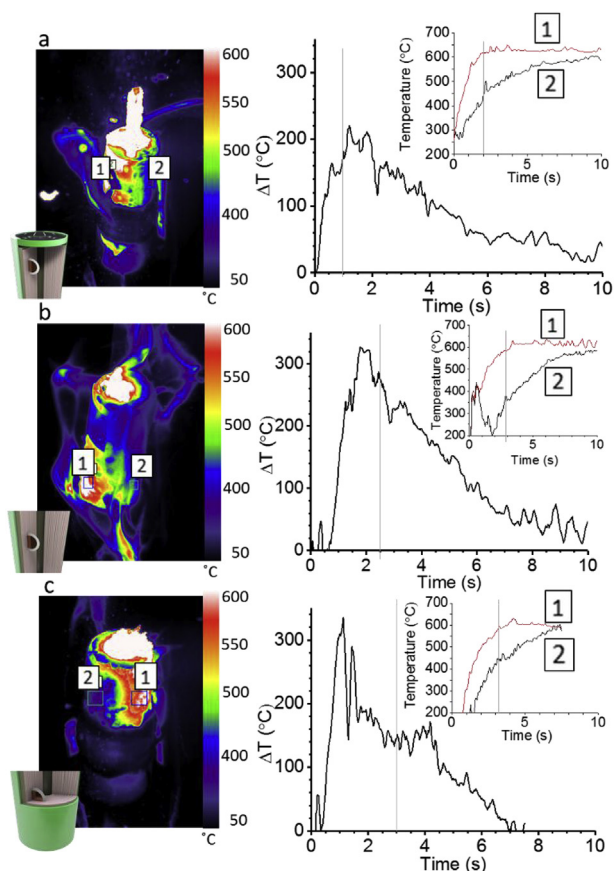
**Fig. 4.** (Left) Thermal images with marked measurement regions [1,2] and (right) plot of temperature difference between regions [1,2], with raw temperature measurements inset for a BV cell with the ISC device 6 layers deep at (a) the top with the cell oriented upright, (b) the middle with the cell oriented upright, and (c) the bottom with the cell oriented upside down showing the BV. The gray lines in the plots designate the time to which the thermal images correspond. Movies of (a), (b) and (c) are provided as Supplementary Movies 2, 6, and 7.

The maximum surface temperature reached will also decide the thermal requirements of the heatsink or insulator material placed between cells in a module. The total heat output from a cell during thermal runaway, as well as the fraction of heat stemming from the casing of the cell and its ejected contents, is also critical to know when engineering a safe module design. In this section, temperature gradients across the surface of failing cells with a known location of thermal runaway initiation are characterized, as well as the influence of location of failure initiation on the overall heat output and the distribution of heat output from the casing of the cell and its ejected contents.

*Surface temperature:* In Fig. 4, the temperature on the surface region closest to the ISC device is compared to the temperature on the opposite side of the cell shortly after initiation of thermal runaway for cells with an ISC device 6 layers deep, at the top, middle and bottom (Fig. 4a–c). The maximum temperature reached at the surface of each cell is between 600 °C and 650 °C, which occurred at the surface directly in line with the position of the ISC device. The location of the point of initiation was consistently identified as subsurface to the region that reaches the highest temperature. Hence, the ISC device can be used to determine the surface location that experiences the greatest thermal abuse. During thermal runaway, there was a large temperature gradient across the surface of each cell. For example, in Fig. 4a–c the temperature was measured on the side of the cell corresponding to the location of the ISC device and was compared to the opposite side circumferentially. The temperature difference between both sides was plotted and

showed that, following thermal runaway, there existed a circumferential temperature difference of > 200 °C. As seen in a previous study [12], the hotspot formed at the ISC device extends internally towards the vent as the fluidized material flows from the point of initiation in the direction of the pressure drop. Here, that flow of material towards the vent caused a hot spot to form on features of the casing that obstructed it (i.e. deflected the escaping flow), as seen in the thermal images in Fig. 4a and c. It's clear that the location of initiation influences the surface temperature of the cell, it's susceptibility to incur a breach at certain locations, and hence the risks posed by the cell inside a battery system. It is also important to determine whether the location of the ISC device (which mimics the effect of a defect causing a short) influences the total quantity of heat output, as well as the distribution of heat output from the casing of the cell and its ejected contents. This will be discussed in the following section.

Supplementary video related to this article can be found at https://doi.org/10.1016/j.jpowsour.2019.01.077.

*Total and fractional heat output:* The fractional thermal runaway calorimeter (FTRC) described in a previous study [6] was used to measure the total heat output from a single cell and discern the fraction of heat that stemmed from the cell casing (red in Fig. 5a), the material ejected from the positive end of the cell (blue in Fig. 5a), and material ejected from the negative end of the cell (black in Fig. 5a). This setup enabled direct comparison between the total and fractional heat output from cells for various positions of the ISC device and cell designs. In Fig. 5b–e, the influence of radial and longitudinal positioning of the ISC device for BV and NBV cells on the total and distribution of heat output between ejected and non-ejected materials is presented. The complete data-set from these experiments, including standard deviations and post-test cell masses, is provided in Table 1.

*Influence of longitudinal position of initiation on heat output:* The ISC device was placed 6 layers radially into the electrode assembly near the top, middle and bottom of the cell. Fig. 5b and c shows the total and fractional heat outputs for each case in BV and NBV cells, respectively. The associated standard deviations are presented in Table 1. The longitudinal location of the ISC device did not appear to significantly affect the total quantity of heat emitted or the fraction of heat emitted from the casing of the cells, but, as expected, had a large effect on the fraction of heat ejected from the top and bottom of the cells. For BV cells, when the ISC device was placed near the top an average of 51.1% of the total heat was emitted from contents ejected through the top, whereas when the ISC device was placed near the bottom, only 32.5% of heat was ejected through the top. Similarly, the fraction of heat that was emitted from material ejected from the bottom of BV cells increased from an average of 11.7%–31.4% between changing the location of the ISC device from the top to the bottom. This behavior is also amplified by a higher quantity of cells undergoing breaching near the location of the ISC device as shown in Fig. 2d (e.g. when the device is placed near the top, there is a higher risk of a top breach occurring). A similar relationship between proximity of the ISC device to one end, and the mass of materials ejected at that end, was observed; the average masses ejected through the top of the cell when the ISC device was positioned at the bottom, middle and top, were 5.3 g, 8.5 g, and 10.2 g, respectively. The average masses ejected through the BV for the ISC device positioned at the bottom, middle, and top, are 4.8 g, 3.0 g, and 2.5 g, respectively. This correlation between the quantity of mass and heat ejected is expected, since the active material was exposed to an oxygen rich environment and would have continued to generate heat for a short period of time outside the cell. For NBV cells, the proximity of the ISC device to the bottom of the cell appeared to increase the fraction of heat ejected from the bottom. This was due to the increased risk of cells undergoing a bottom breach (0% for the ISC at the top, compared to 25% for the ISC at the bottom), as shown in Fig. 2e. This demonstrates that for both BV and NBV cells, the proximity of the ISC device to either end of the cell increases the fraction of the total heat that is ejected at that end.
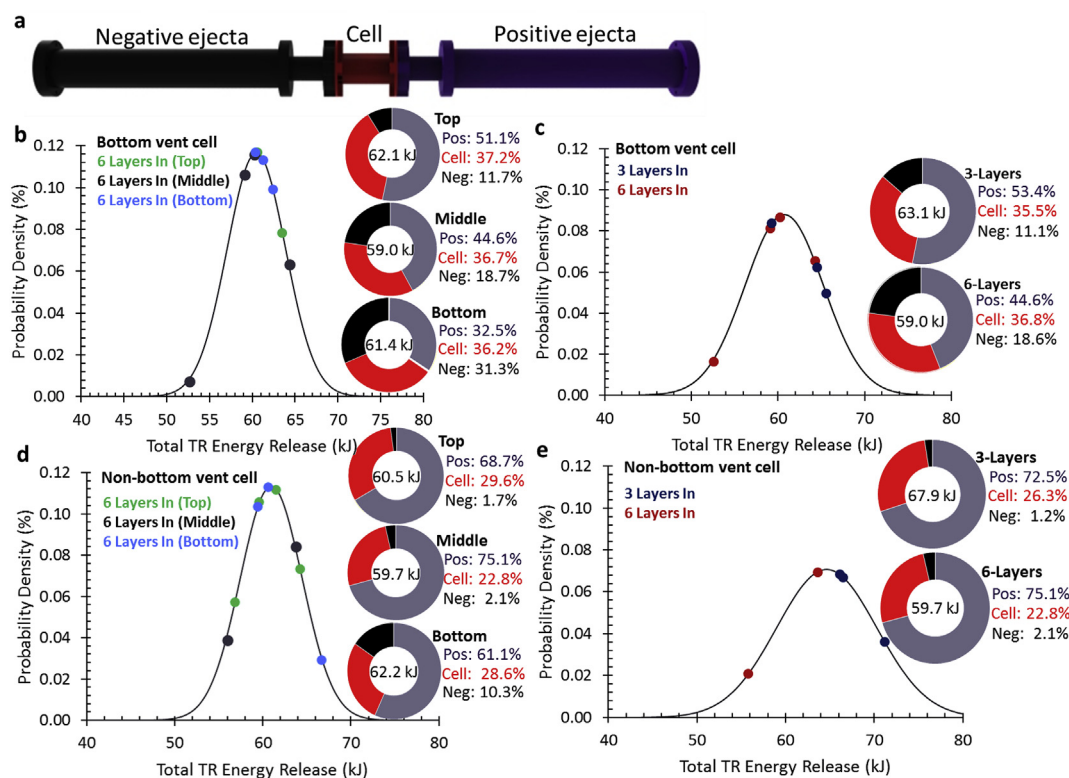
**Fig. 5.** (a) Color coded illustration of the FTRC for reference. (b) Statistical plot showing the heat output and averaged distribution of heat output for BV cells with the ISC device placed 6 layers deep at the top, middle and bottom, and (c) 3 layers deep and 6 layers deep at the middle; and (d) for NBV cells with the ISC device place 3 layers deep and 6 layers deep at the middle, and (e) 6 layers deep at the top, middle and bottom. (For interpretation of the references to color in this figure legend, the reader is referred to the Web version of this article.)

*Influence of radial position of initiation on heat output:* In Fig. 5c and e, the total and fractional heat output for ISC devices placed 6 and 3 layers deep for BV and NBV cells, respectively. An increase in the total heat output is observed for the ISC device positioned 3 layers deep compared to 6 layers deep. The average heat output for 3 layers deep in a BV cell is 6.9% more than 6 layers deep, and for NBV cells the average heat output is 13.9% greater than for 6 layers deep. This behavior may be related to the difference in the flow path of ejecting material (being more direct when the ISC occurs 6 layers deep) and the local dissipation of heat (with more thermal mass surrounding the ISC device 6 layers deep). The radial location of the ISC device also appears to affect the fractional heat output for BV cells, where more heat is ejected through the base of the cell for 6 layers deep than 3 layers deep (18.6% compared to 11.1%). This may be caused by there being a more direct path for fluidized material to escape when the short occurs deeper into the electrode assembly. Conversely, less heat is ejected through the top of the cell for 6 layers deep than 3 layers deep, while the heat emitted from the cell casing is similar for both cases (ca. 36%).

*Influence of bottom vent on heat output:* The most significant impact of the bottom vent is on the fractions of heat output from the casing and its ejected contents, as well as the quantity of mass ejected (Table 1). The presence of a bottom vent leads to a reduction in the mass of material ejected and an increased fraction of heat emitted from within the casing of the cell. On average, a post-thermal runaway BV cell weighed *ca.* 24% (5 g) more than an NBV cell (Table 1). Further, of the total quantity of heat generated, BV cells produced *ca.* 9% more heat in the casing of the cell and ejected less heat overall. The enhanced pressure relief in BV cells is expected to have reduced the pressure drop between the inside of the cell and atmosphere during TR, and hence reduced the driving force for materials to eject. That is to say, a reduction in the ejection of thermal mass and exothermically decomposing material caused more heat to be generated within the casing and

less heat to be dissipated elsewhere. This result demonstrates the safety benefits of improving pressure relief in 18650 cells. The concentrated heat generation within the casing of 18650 BV cells may also have safety advantages for some module designs that are particularly vulnerable to ejected heat sources, albeit additional considerations for the bottom vent feature are needed, such as a head spacing on the bottom as well as the top of the module.

### 3.4. Modelling thermal runaway to identify vulnerabilities

3D thermal runaway models were constructed to further elucidate the causes of high-risk breach scenarios arising from local thermal runaway (Fig. 2). The model parameters are based on the thermal measurements outlined above. The radial, longitudinal, and circumferential rates of propagation of thermal runaway from the point of initiation are approximated from the numerous high-speed X-ray imaging movies of the ISC device activating and were used in the model. The progression of the modelled reaction zone for when the ISC device is placed near the top, middle, and bottom is shown in Fig. S3 of Supplementary Material. The reaction zone propagated fastest in the longitudinal and azimuthal directions [10,28], forming a hollow cylindrically-shaped reaction zone seen between 0.4 s and 0.6 s (Fig. S3 in Supplementary Material). The reaction reached completion in a shorter time when the ISC was located at the middle, as seen by the reaction zone encompassing the entire cell 1 s after initiation of thermal runaway (Fig. S4a in Supplementary Material), whereas only ca. 90% of the cell volume was encompassed when the ISC device is placed at the ends of the cell (Figs. S4a and c in Supplementary Material). This stems from the reaction front being able to propagate equally in both directions when initiation occurs at the middle, whereas when initiation occurs near either end, the reaction front halts at the end of the electrode assembly while continuing uninterrupted in the opposite direction.

**Table 1**
Data on the total heat output, the fractional heat distribution, cell masses pre and post-thermal runaway (TR), and the distribution of post-thermal runaway masses between ejected and non-ejected contents, for the four positions of the ISC device implanted into bottom vent (BV) and non-bottom vent (NBV) 18650 cells. Standard deviation for each averaged value are also provided. Color coding (red, blue, black), reflects the respective locations of measurements within the calorimeter from Fig. 5a.

|  | 6 layers: Top | | 6 layers: Middle | | 6 layers: Bottom | | 3 layers: Middle | |
|---|---|---|---|---|---|---|---|---|
|  | BV | NBV | BV | NBV | BV | NBV | BV | NBV |
| Avg. total heat $E_{tot}$ (kJ) | 62.1 | 60.5 | 59.0 | 59.7 | 61.4 | 62.2 | 63.1 | 67.9 |
| Std. Dev. | 2.1 | 3.1 | 4.8 | 5.5 | 1.0 | 3.9 | 3.4 | 5.5 |
| Avg. Percent $E_{Cell\ Body}$ | 37.2 | 29.6 | 36.7 | 22.9 | 36.2 | 28.6 | 35.5 | 26.3 |
| Std. Dev. | 8.3 | 4.2 | 7.3 | 6.5 | 1.7 | 8.0 | 7.1 | 6.5 |
| Avg. Percent $E_{Ejecta\ \&\ Gas}$ (+) | 51.0 | 68.7 | 44.6 | 75.1 | 32.5 | 61.1 | 53.4 | 72.5 |
| Std. Dev. | 22.0 | 4.5 | 17.2 | 5.6 | 4.3 | 14.2 | 19.4 | 5.6 |
| Avg. Percent $E_{Ejecta\ \&\ Gas}$ (-) | 11.7 | 1.6 | 18.6 | 2.1 | 31.4 | 10.3 | 11.2 | 1.2 |
| Std. Dev. | 13.7 | 0.7 | 12.1 | 1.0 | 3.2 | 7.9 | 16.0 | 1.0 |
| Avg. Cell Mass (Pre-TR) (g) | 47.3 | 47.1 | 47.2 | 47.0 | 47.3 | 47.0 | 47.2 | 47.8 |
| Std. Dev. | 0.0 | 0.1 | 0.1 | 0.0 | 0.0 | 0.0 | 0.2 | 0.0 |
| Avg. Cell Mass (Post-TR) (g) | 25.0 | 21.8 | 25.7 | 20.3 | 27.2 | 21.9 | 24.3 | 19.3 |
| Std. Dev. | 2.3 | 1.4 | 2.0 | 0.7 | 0.7 | 5.1 | 3.9 | 0.7 |
| Avg. Ejecta Mass (+) (g) | 10.2 | 14.7 | 8.5 | 15.6 | 5.3 | 11.6 | 10.5 | 16.3 |
| Std. Dev. | 3.0 | 1.5 | 4.0 | 1.4 | 0.7 | 6.4 | 5.3 | 1.4 |
| Avg. Ejecta Mass (-) (g) | 2.5 | 0.0 | 3.0 | 0.3 | 4.8 | 1.5 | 1.6 | 0.2 |
| Std. Dev. | 0.1 | 0.0 | 3.1 | 0.1 | 1.9 | 1.5 | 2.7 | 0.1 |
| Casing Thickness (µm) | 220 | 250 | 220 | 250 | 220 | 250 | 220 | 250 |
| Cell count | 2 | 4 | 4 | 2 | 3 | 3 | 3 | 3 |

Therefore, the rate of heat generation for the middle position is expected to surpass the top and bottom positions when the reaction front is halted at one end, but the total quantity of heat produced upon completion is expected to be similar, as observed experimentally in Fig. 5.

*Influence of longitudinal position of initiation on internal and surface temperatures:* The effects of the reaction zone propagating from the three different positions on the internal and surface temperatures are shown in Fig. 6 and the averaged internal and surface temperatures are plotted in Fig. 7. The location of initiation had a significant influence on the temporal internal and surface temperatures where initiation at the ends of the cell lead to higher temperatures at an early stage in the thermal runaway process, compared to when thermal runaway is initiated at the middle. Comparing scenarios where the initiation occurred at the top and at the middle of the cell in Fig. 6a and b, it is observed that after 0.6 s following initiation at the top, the maximum surface temperature of the cell was > 300 °C greater than the cell where initiation occurred at the middle. Within the first 1 s following initiation of thermal runaway, the highest surface temperatures were consistently achieved for when initiation occurred near the bottom of the cell (Fig. 6c). Further, the location of initiation also determined the temperature difference across the surface of the cells, where the middle position resulted in a more homogeneous surface temperature profile than the end positions. For example, between 0.8 s and 1 s in Fig. 6a (top), the top of the cell reached 650 °C, while the bottom of the cell remained at room temperature, but in Fig. 6b (middle) the maximum temperature was *ca.* 400 °C while the rest of the cell was > 200 °C.

The maximum and average surface temperature for each location of initiation in Fig. 6 is plotted in Fig. 7. Surface temperatures were consistently lower when initiation occurred at the middle. This stems from the different geometry of thermal and reactive mass that the propagation front observes. In the case of initiation occurring near the middle of the cell, the propagation continued in both longitudinal directions, equally, until all reactive material broke down. Further, heat generated from the middle position dissipated in both longitudinal directions, thereby helping reduce local temperatures and homogenize the temperature profile across the surface. This reduced the rate of propagation of thermal runaway at the early stages, as seen by the relatively small reaction zone at 0.4 s in Fig. S4b in Supplementary Material. When initiation occurred near either end of the cell, the thermal and reactive mass in one direction was reduced. The heat that was generated from a short at either end is mostly dissipated via conduction in one direction only (away from that end). The reduced heat dissipation in this case resulted in a more rapid temperature rise at the point of initiation and accelerated the propagation of thermal runaway. Therefore, to test temperature-related vulnerabilities at the top or bottom of cells or the corresponding regions in battery modules, it is advised to initiate thermal runaway at the appropriate end of the cell.

*Influence of longitudinal position of initiation on bursting pressure:* An example of a temperature-dependent vulnerability is the bursting pressure of the cell, which is a function of the temperature-dependent tensile strength of the cell's steel casing. The tensile strength of a common structural steel (S350GD) as a function of temperature was applied to the surface temperature profiles in Fig. 6 and is presented in Fig. 8. For a 3.35 Ah 18650 cell, it is expected that *ca.* 6 L of gas were generated during thermal runaway [5]. If 6 L of gas is contained within the 18650 casing volume (0.01674 L), and assuming the vents were prevented from relieving pressure, the internal pressure would exceed 30 MPa which is enough to cause the cell to burst even when the casing is at room temperature, where the bursting pressure is *ca.* 9 MPa (Fig. 8) for the 220 µm thick casing. As the tensile strength of steels rapidly decreases at temperatures > 100 °C, the bursting pressure will also decrease. Hence, hotspots that form on the casing are most susceptible to bursting. At temperatures between 400 °C and 800 °C, the bursting pressure becomes particularly sensitive to temperature (see tensile strength data in Supplementary Material), where even small differences in surface temperature can lead to large differences in the bursting pressure in this range. As seen in Fig. 8, initiation of thermal runaway near the ends of the cells resulted in the lowest bursting pressure which corresponded to the higher maximum temperatures achieved in Fig. 6. The bursting pressure of the cell dropped below 1.5 MPa after 0.6 s following initiation of thermal runaway near the top and bottom of the cells, whereas the lowest bursting pressure of *ca.* 2.5 MPa occurred after 1 s for when thermal runaway initiated near the middle. The additional heat dissipation for the middle initiation scenario kept the surface temperature relatively low and helped maintain a higher casing tensile strength overall. The higher casing tensile strength for the middle initiation could withstand a higher internal pressure and hence a lower flowrate of escaping gases. This reduced the risk of the cell bursting in the event that the flowrate of escaping gases was hindered, as seen in a previous study [9]. Hence, if a cell or module vulnerability against a breach at a certain location needed to be tested, positioning the ISC device at a longitudinal and radial position that corresponded to the region of interest is advised. Thinner casings are advantageous for purposely inducing breaches at certain locations (for testing vulnerabilities of modules), but for improved safety, thicker casing designs for improved heat dissipation and increased bursting pressures are recommended.

### 3.5. A discussion on cell safety and testing

Aside from changes in the chemistry of electrodes and electrolytes, which are beyond the scope of this study, the mechanical design of cells plays an important role in the safety of cells and modules. When thermal runaway occurs, the mechanical design of the casing, vents, and other safety features are what control the distribution of hot gases
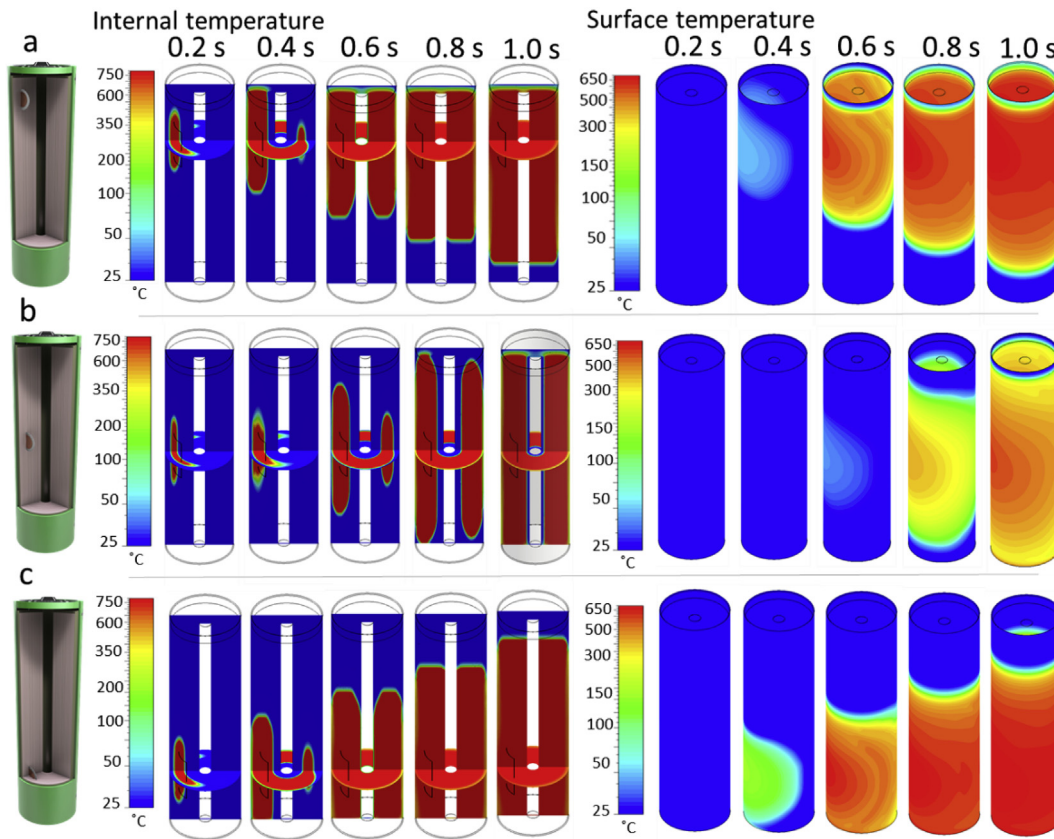
**Fig. 6.** Evolution of the internal and surface temperatures over 1 s following initiation of thermal runaway when the ISC was located (a) near the top, (b) at the middle, and (c) near the bottom of an 18650 geometry.
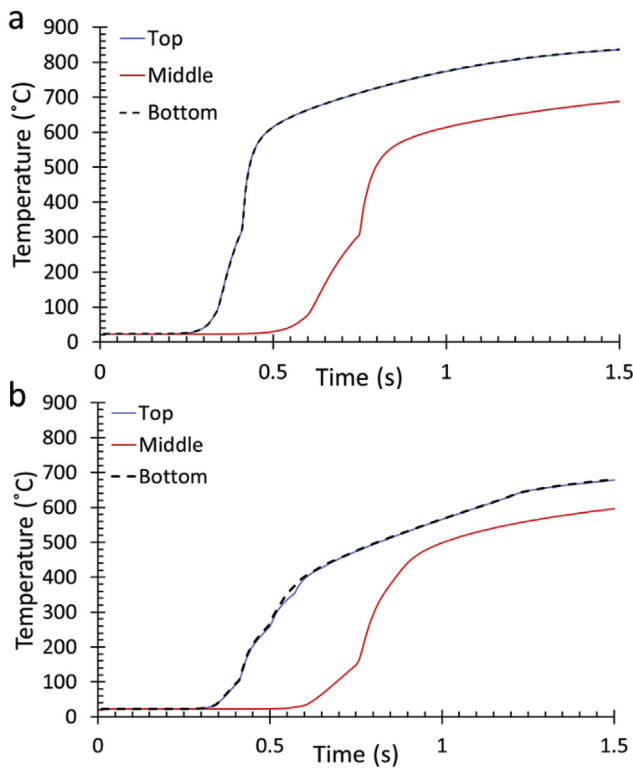


**Fig. 7.** Modelled thermal runaway plots showing (a) the max surface temperature and (b) the average surface temperature for when the ISC device is placed at the top, middle and bottom of the 18650 cell.

and materials, as well as the dissipation of heat into the environment. Most commercial 18650 cells are designed to eject heat and debris in one direction only, through the top vent of the cell, and battery modules are designed to accommodate this. Although rare, certain adverse and unpredictable phenomena can lead to a divergence of this behavior. For example, it was shown in a previous study [9] that if the electrode assembly shifts and clogs the vent during thermal runaway the 18650 cell can violently burst or undergo a pressure-induced breach. It is the bursting and side-wall breaches of cells that most often defeat safety features in battery modules and lead to cell-to-cell propagation of thermal runaway. The ISC device can be used to reliably replicate the most unfavorable and otherwise unpredictable adverse failure mechanisms, such as bursting and side-wall breaches. This is a very powerful tool for identifying vulnerabilities on the cell level (e.g. identifying regions most likely to incur a breach), as well as on the module level (e.g. intentionally causing breaches at a certain location to test the efficacy of a module design in preventing cell-to-cell propagation). For example, here we identified deflection points such as the spingroove and base plate as regions most susceptible to breaching. If a battery pack is being designed for a mission critical application (e.g. the life support system of a space suit) a matrix of high-energy density cells with selectively located ISC devices could be used to improve confidence that the current module design can withstand worst-case internal shorting scenarios.

## 4. Conclusion

By linking internal dynamics to external risks, a comprehensive description of high-risk failure scenarios of 18650 cells, their causes, and their consequences, was developed. An internal short circuiting (ISC) device was placed at different longitudinal and radial positions
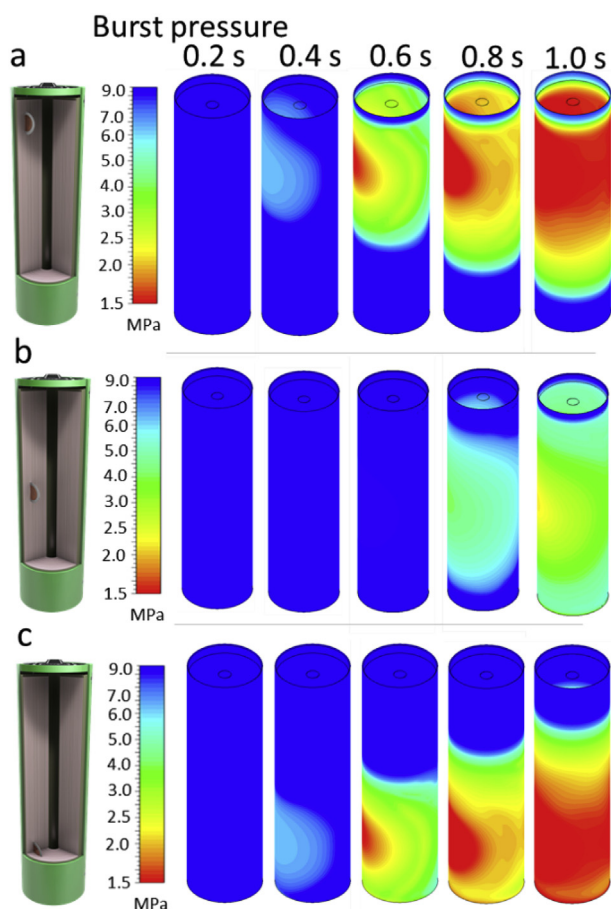
**Fig. 8.** Surface profiles of bursting pressures over 1 s following initiation of thermal runaway when the ISC was located (a) near the top, (b) at the middle, and (c) near the bottom of an 18650 geometry, based on the reduction in tensile strength of steel at increased localized temperature.

within the cells to test the effect of location of thermal runaway initiation on the failure mechanism of the three cell designs where high-risk failure mechanisms such as bursting and breaching were of primary interest. It was shown that by using an ISC device, the most likely failure scenarios for inducing bursting and breaching of the cell casing can be intentionally induced. For example, it was demonstrated that by initiating thermal runaway near the top or bottom of an 18650 cell, the risk of breaching at the respective end is significantly increased. Using this method, a risk-map outlining the conditions necessary for certain high-risk failure mechanisms was generated.

The external risks posed by initiating failure at different locations were explained with respect to surface temperature profiles, total heat output, as well as the fractional heat generated from the ejected and non-ejected contents. The location of thermal runaway initiation influenced the quantity of heat and mass ejected from the cell, where the highest surface temperatures and the greatest quantity of heat was ejected at the end of the cell where the ISC device was placed. This approach allowed comparisons between different cell designs to be drawn; the introduction of a bottom vent on the 18650 cell was found to significantly reduce the quantity of ejected mass and heat during thermal runaway by more effectively relieving pressure and reducing the pressure drop from inside to outside the cell.

The cause of the adverse failure mechanisms and their link to the location of thermal runaway initiation were explained by using high-speed synchrotron X-ray imaging and computational modelling. The interaction between the mechanical design of the cells and the internal structural dynamics played a pivotal role in determining the external

risks. High-speed X-ray imaging revealed that the active materials within the cell underwent a phase change from solid to liquid during thermal runaway and ejected with fluid-like properties. Regions that deflected the escaping flow of hot material, such as the spin-groove and the base plate, were found to be at the highest risk of breaching. A thermal runaway model was developed using parameters extracted from the X-ray images as well as thermal measurements from infrared imaging and calorimetry, to further elucidate why certain regions were more prone to breaching than others. The thermal runaway model revealed that, due to differences in the heat dissipation properties at different locations along the electrode assembly, the surface temperature profiles significantly varied with location of thermal runaway initiation. This was due to reduced heat dissipation from the reaction zone when thermal runaway initiated near either end of the cell. Consequently, the bursting pressure of the casing at the exception hotspots generated when initiation of thermal runaway occurred near the top or bottom of the cell, was significantly lower than the bursting pressure achieved when initiation took place near the middle of the cell.

These results helped identify the vulnerable regions of the cell (around the spin-groove and base plate) and highlight that additional support is needed, such as using more thermally stable alloys or thicker steel to enhance heat dissipation and improve the tensile strength during thermal runaway. This work also demonstrates the application of ISC devices for intentionally inducing worst-case thermal runaway scenarios to test the efficacy of next generation cell or module designs in avoiding catastrophic failure. And finally, the combination of techniques presented here (high-speed X-ray imaging, fractional thermal runaway calorimetry, and thermal imaging) was established as a powerful diagnostic approach for developing comprehensive descriptions of battery failure and associated risks. The detailed information of thermal and structural dynamics is not only useful for informing engineering design, but can also be used to enhance safety-focused multiphysics models of Li-ion batteries.

## Appendix A. Supplementary data

Supplementary data to this article can be found online at https://doi.org/10.1016/j.jpowsour.2019.01.077.

## References

[1] J. Lamb, C.J. Orendorff, E.P. Roth, J. Langendorf, J. Electrochem. Soc. 162 (2015) A2131–A2135.

[2] Z. Chen, Y. Qin, Y. Ren, W. Lu, C. Orendorff, E.P. Roth, K. Amine, Energy Environ. Sci. 4 (2011) 4023–4030.

[3] D.P. Finegan, M. Scheel, J.B. Robinson, B. Tjaden, M. Di Michiel, G. Hinds, D.J.L. Brett, P.R. Shearing, Phys. Chem. Chem. Phys. 18 (2016) 30912–30919.

[4] R. Spotnitz, J. Franklin, J. Power Sources 113 (2003) 81–100.

[5] C. Orendorff, J. Lamb, L.A. Steele, S. Spangler, J. Langendorf, Sandia Report, Sandia National Labs, Sandia National Labs, 2016.

[6] W. Walker, J. Darst, D. Finegan, G. Bayles, K. Johnson, E. Darcy, S. Rickman, J. Power Sources, (2019) (in press).

[7] X. Feng, M. Fang, X. He, M. Ouyang, L. Lu, H. Wang, M. Zhang, J. Power Sources 255 (2014) 294–301.

[8] D.P. Finegan, M. Scheel, J.B. Robinson, B. Tjaden, I. Hunt, T.J. Mason, J. Millichamp, M. Di Michiel, G.J. Offer, G. Hinds, D.J.L. Brett, P.R. Shearing, Nat. Commun. 6 (2015).

[9] D.P. Finegan, E. Darcy, M. Keyser, B. Tjaden, T.M.M. Heenan, R. Jervis, J.J. Bailey, N.T. Vo, O.V. Magdysyuk, M. Drakopoulos, M.D. Michiel, A. Rack, G. Hinds, D.J.L. Brett, P.R. Shearing, Adv. Sci. (2017) 1700369.

[10] D.P. Finegan, E. Darcy, M. Keyser, B. Tjaden, T.M.M. Heenan, R. Jervis, J.J. Bailey, R. Malik, N.T. Vo, O.V. Magdysyuk, R. Atwood, M. Drakopoulos, M. DiMichiel, A. Rack, G. Hinds, D.J.L. Brett, P.R. Shearing, Energy Environ. Sci. 10 (2017) 1377–1388.

[11] C.F. Lopez, J.A. Jeevarajan, P.P. Mukherjee, J. Electrochem. Soc. 162 (2015) A1905–A1915.

[12] D.P. Finegan, B. Tjaden, T.M.M. Heenan, R. Jervis, M.D. Michiel, A. Rack, G. Hinds, D.J.L. Brett, P.R. Shearing, J. Electrochem. Soc. 164 (2017) A3285–A3291.

[13] J. Lamb, C.J. Orendorff, J. Power Sources 247 (2014) 189–196.

[14] S. Wilke, B. Schweitzer, S. Khateeb, S. Al-Hallaj, J. Power Sources 340 (2017) 51–59.

[15] C.F. Lopez, J.A. Jeevarajan, P.P. Mukherjee, J. Electrochem. Soc. 162 (2015) A2163–A2173.

[16] A.W. Golubkov, D. Fuchs, J. Wagner, H. Wiltsche, C. Stangl, G. Fauler, G. Voitic, A. Thaler, V. Hacker, RSC Adv. 4 (2014) 3633–3642.

[17] P. Ribiere, S. Grugeon, M. Morcrette, S. Boyanov, S. Laruelle, G. Marlair, Energy Environ. Sci. 5 (2012) 5271–5280.

[18] J. Deng, C. Bae, J. Marcicki, A. Masias, T. Miller, Nature Energy 3 (2018) 261–266.

[19] J. Zhu, T. Wierzbicki, W. Li, J. Power Sources 378 (2018) 153–168.

[20] R. Zhao, J. Liu, J. Gu, Appl. Energy 173 (2016) 29–39.

[21] X. Feng, L. Lu, M. Ouyang, J. Li, X. He, Energy 115 (2016) 194–208.

[22] C.J. Orendorff, E.P. Roth, G. Nagasubramanian, J. Power Sources 196 (2011) 6554–6558.

[23] M. Zhang, J. Du, L. Liu, A. Stefanopoulou, J. Siegel, L. Lu, X. He, X. Xie, M. Ouyang, J. Electrochem. Soc. 164 (2017) A3038–A3044.

[24] S. Santhanagopalan, P. Ramadass, J. Zhang, J. Power Sources 194 (2009) 550–557.

[25] M. Keyser, E. Darcy, D. Long, A. Pesaran, in, Alliance for Sustainable Energy, LLC, 2015, pp. U.S. patent 9142829B9142822.

[26] M. Vollmer, K.-P. Mollmann, Infrared Thermal Imaging: Fundamentals Research and Applications, Wiley - VCH, 2010.

[27] G.-H. Kim, K. Smith, K.-J. Lee, S. Santhanagopalan, A. Pesaran, J. Electrochem. Soc. 158 (2011) A955–A969.

[28] G.-H. Kim, A. Pesaran, R. Spotnitz, J. Power Sources 170 (2007) 476–489.

[29] J. Outinen, P. Makelainen, Structures in Fire - Second International Workshop, (2002).